

Aerodynamics of Finite Cylinders in Quasi-Steady Flow

Daniel T. Prosser* and Marilyn J. Smith†

School of Aerospace Engineering, Georgia Institute of Technology, Atlanta, GA

The aerodynamics of finite circular cylinders are important across a broad range of engineering disciplines. However, there currently exists a significant gap in the literature on such bluff bodies, particularly at orientations other than the typical normal and axial flow conditions. This work addresses that gap through high-fidelity numerical experiments, employing large-eddy simulation in the wake, of finite cylinders over a broad range of yaw angles and Reynolds numbers. Though the approach is already well-validated for bluff body flows, additional validation is performed for those cases in which experimental data are available, and sensitivity analysis of the results is also presented. Empirical modeling of the aerodynamics is performed to aid in the development of reduced-order models for pilot training, stability analysis, and flight certification. Key results include quantification of mean and fluctuating force and moment coefficients and shedding frequencies, empirical models of trends in shear layer behavior, and analysis of the sensitivity of these behaviors with respect to surface type, aspect ratio, and Reynolds number.

Nomenclature

α	Angle of attack
β	Yaw angle
c_{pb}	Base pressure coefficient
c_{pM}	Maximum pressure coefficient
c_{ps}	Separation bubble pressure coefficient
D	Cylinder diameter
L	Cylinder length
L/D	Aspect ratio
ϕ	Incidence angle
ϕ_R	Incidence angle at initial reattachment
Re_D	Reynolds number based on diameter
St	Strouhal number, $St = \frac{fD}{U_\infty}$
u, v, w	Velocity components
U_∞	Freestream speed
V	Velocity magnitude, $V = \sqrt{u^2 + v^2 + w^2}$
x_0	Stagnation point position
x_M	Reattachment distance

I. Introduction

Flows around cylinders are pervasive in a wide range of engineering disciplines. Many structures pertinent to industrial applications, including cables, girders, power lines, towers, and skyscrapers, may be represented as long circular cylinders. In such cases, three-dimensional effects are often considered unimportant.¹ However, there exist a number of applications in which short-length finite cylindrical bodies are of interest. One

*Ph.D. Candidate, AIAA Student Member

†Professor, AIAA Associate Fellow

example is in the area of helicopter tethered loads. In these operations, a wide variety of bluff bodies may be transported slung underneath a helicopter by a system of cables, resulting in complex aerodynamic-dynamic interactions of the tethered load, which is also coupled to the response of the tether system and helicopter itself.^{2,3} Typical tethered loads include oil drums and engine canisters, which may be approximately represented as short finite cylinders. Other applications requiring finite cylinder aerodynamics include air drops, store separation, and missile flight.^{4,5}

One of the earliest experimental studies of finite-length cylinders was undertaken by Wieselsberger.⁶ In that investigation, the drag coefficient of finite cylinders in normal flow (the condition in which the curved surface is normal to the flow) was measured over a broad range of Reynolds numbers. Both infinite cylinders (without free ends) and finite cylinders with $L/D = 5$ were studied. It was found that, in the subcritical and transitional regimes, the drag of the finite cylinder was significantly less than the infinite cylinder. However, this difference disappeared at supercritical Reynolds numbers on the order of 10^6 . Additionally, the Reynolds numbers defining the subcritical, transitional, and supercritical flow regimes were similar between the two different aspect ratios, and the magnitudes of drag changes during these transitions were also comparable. Zdravkovich et al.⁷ performed wind tunnel experiments on short cylinders having two free ends, with L/D ranging from two to ten, primarily in the subcritical Reynolds number regime. The observations were similar to those of Wieselsberger, in that decreasing the aspect ratio resulted in a decrease in drag. However, below $L/D = 5$, further decreases in aspect ratio resulted in little if any additional drag decrease. Zdravkovich et al. also measured the yaw moment coefficient, finding considerable variation between trials. The variation was determined to be the result of an asymmetric pressure distribution on the curved face which could shift from side to side in an unpredictable fashion. Additionally, the Strouhal frequency of vortex shedding for $L/D < 5$ was found to be in the range 0.15 – 0.27, but the shedding itself was highly irregular and difficult to assign a single dominant frequency. This behavior was attributed to the highly turbulent and three-dimensional flow interactions occurring with the short cylinder geometry.

In most of the applications identified for small aspect ratio cylinders, it is necessary to resolve the forces and moments not only in normal flow but also in a broad range of other orientations. While the literature on small aspect ratio cylinders in normal flow is sparse, there exists even less information at other orientations. Hoerner⁸ compiled data for cylinders and disks in axial flow (with the flat face normal to the flow). In this orientation, drag was found to decrease abruptly as L/D increased from zero (circular disk) to two, but it then remained approximately constant as L/D was increased further. The abrupt drop in drag may be attributed to a change in shear layer behavior, as it begins to reattach on the curved face around $L/D = 1$. Normal force coefficients have also been compiled by Hoerner⁸ for circular disks over a range of angle of attack from zero to 90 degrees. Similar data are also extant for subsonic flow over missiles,^{4,5} which are cylindrical in cross section but typically have a rounded end with aspect ratios greater than five.

A significant amount of data in the literature exists for infinite cylinders at an angle of incidence. For example, Bursnall⁹ measured the pressure distribution about a circular cylinder at yaw angles from zero to 60 degrees at Reynolds numbers below 5.0×10^5 . Zdravkovich¹ has presented a rather comprehensive review of this and more recent experiments. Many of these focus on the validity of the *independence principle*, or the theory that the flow in a plane normal to the circular cross-section may be analyzed independently of the axial flow component. The theory was presented formally by Sears¹⁰ and is based on the assumptions that the flow is two-dimensional and laminar. Therefore, the theory breaks down at the onset of separation and in three-dimensional flows, as in the case of a short finite cylinder with free ends. Nonetheless, the theory has been shown to be reasonably accurate for real cylinders in some cases, depending on the aspect ratio and end conditions.^{9,11}

There remains a marked lack of treatment of short circular cylinders in more than just one or two orientations. The majority of studies to date have focused on infinite cylinders in normal flow. There are fewer, but still a considerable number, of investigations of infinite cylinders inclined to the flow and short finite cylinders in normal or axial flow; however, little if any information is available on short finite cylinders in other orientations. This gap presents significant difficulty in predicting the behavior of these types of geometries in applications such as tethered load operations and air drops. The goal of the current work is to begin to close this gap via high-fidelity hybrid RANS-LES simulations of short cylinders in static orientations over a broad range of inclination angles. Integrated quantities and shedding frequencies are computed, and the computations are validated against experimental data, where available. The numerical approach allows significant insight into the changes in flow behavior which affect the quasi-steady forces and moments. For the purpose of reduced-order aerodynamic modeling applicable to simulation environments, empirical models

of the quasi-steady behavior are presented along with guidance as to the conditions in which they may be applied.

II. Configurations

In selecting the configurations to study, several criteria were considered. First, the configurations should be in a range of aspect ratios that are representative of common tethered loads. This resulted in cylinders of very low aspect ratio with $L/D = 1 - 2$. Reynolds numbers over a relatively broad range of $10^5 - 10^6$ were selected, which are typical of model-scale (as in a wind tunnel test) to full-scale tethered loads. 11 different discrete yaw angles in the range $0^\circ \leq \beta \leq 90^\circ$ were investigated. The full summary of test conditions is presented in Table 1.

Table 1: Cylinder dimensions and flow conditions

No.	L (m)	D (m)	Re_D	β ($^\circ$)
1	0.2191	0.2191	0.96×10^5	0, 2.5, 5, 10, 20, 30, 45, 60, 70, 80, 90
2	0.2191	0.2191	1.00×10^6	0, 10, 30, 70, 90
3	0.4382	0.2191	1.56×10^5	0, 2.5, 5, 10, 20, 30, 45, 60, 70, 80, 90
4	0.4382	0.2191	0.96×10^5	0, 30, 80, 90
5	0.4382	0.2191	1.00×10^6	0, 10, 30, 70, 90

The cylinders are *canonical* geometries; i.e., they are perfect cylinders without any surface imperfections or wind tunnel mounting apparatus modeled in the grid, but they are representative geometries for the tethered loads application as well as many others. The yaw angle is defined as zero when the cylinder is in the *normal flow* orientation; that is, with the stagnation point at the center of the curved face. A yaw angle of 90° occurs with stagnation point at the center of the flat face, or the *axial flow* orientation. The convention for the relationship between the wind axes and body axes, with the yaw angle β and angle of attack α illustrated, is presented in Fig. 1. In all cases considered in this work, the angle of attack is held to zero while the yaw angle is varied.

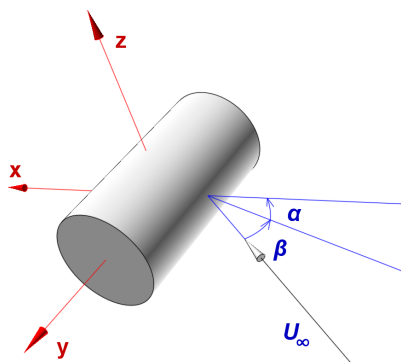


Figure 1: Convention for axes and illustration of the aerodynamic angles α and β .

III. Numerical Experiment Methodology

In this work, numerical experiments are undertaken to evaluate the aerodynamics of finite cylinders. This approach is selected because of the rich flow field information that it provides at no additional cost, which makes it possible to determine basic fluid flow phenomena that influence the integrated forces and moments. Of course, with any numerical approach, it is important to validate the computations and use established best practices to ensure that the results are accurate. The current methodology has been leveraged from prior algorithm development by Lynch¹² and Shenoy.¹³ FUN3D, a legacy unstructured CFD solver developed by NASA,¹⁴ is employed to resolve the bluff body flow fields. FUN3D solves the incompressible or compressible Reynolds-Averaged Navier-Stokes (RANS) equations on mixed-element unstructured grids. The solver is

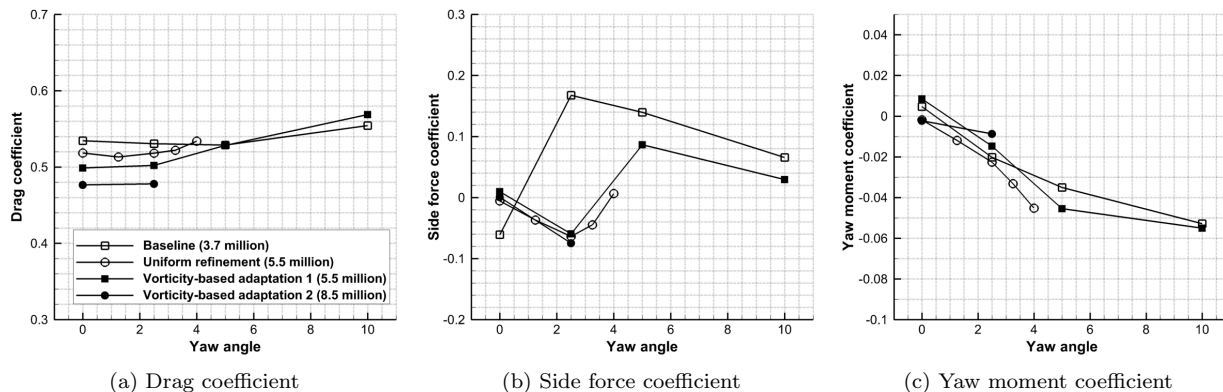


Figure 2: Grid sensitivity study, $L/D = 1$ at low β , $Re_D = 3.2 \times 10^5$.

second-order accurate in space and between second- and third-order accurate in time, which is important for resolving large eddies in the wakes of bluff bodies. Pure RANS solutions are known to be inadequate for flows around airfoils at high angles of attack and other bluff bodies.^{15,16} To mitigate this issue, a hybrid turbulence approach is applied, in which the $k-\omega$ SST two-equation near-wall RANS model is blended with large-eddy simulation (LES) in the wake where the largest turbulence scales may be resolved by the grid.¹² This approach has been demonstrated to accurately predict bluff body flows in a wide range of applications, including airfoils at high angles of attack and in reverse flow,¹⁵ semi-infinite cylinders,¹² and rectangular prisms.¹⁷ The latter work has demonstrated significantly improved predictions of side force and yawing moment of three-dimensional rectangular prisms over a broad range of yaw angles relative to other computations employing RANS or algebraic turbulence models.^{16,18}

In the current work, cylinders are studied in flows at very low Mach numbers (below 0.1), so the incompressible solver path is taken in FUN3D to ensure rapid convergence. Rather than apply preconditioning to the compressible Navier-Stokes equations, the incompressible path in FUN3D is implemented via Chorin's method of artificial compressibility,¹⁹ which reduces computational cost, as the energy equation need not be solved in this approach. The overset grid method is applied, in which near-body cylinder grids are placed on top of a background grid representing a wind tunnel test section. This method allows the same set of grids to be used in multiple orientations. Overset capability is afforded by the SUGGAR++²⁰ and DiRTlib²¹ libraries, which determine blanked cells, donors and recipients at overset boundaries, and interpolate data from grid to grid. Inviscid fluxes are resolved using Roe's flux-difference splitting scheme, while temporal integration is performed via an implicit, time-accurate backwards-difference scheme.

III.A. Computational grids

Grids were created for the finite cylinders applying best practices for similar bluff body configurations with the hybrid RANS-LES turbulence approach.^{12,15,22,23} Though the grids are unstructured, previous investigations have demonstrated the importance of wall-normal-aligned prismatic elements to accurately resolve gradients in the boundary layer.¹² Thus, the topology of the near-body grids is mixed with prismatic elements in the boundary layer and tetrahedral elements elsewhere. 35 or more prismatic cells are included in the boundary layer region, with viscous wall spacing $y^+ < 1$. These boundary layer grid characteristics have been selected to ensure accuracy in predictions of separation and reattachment locations which have been evaluated in prior work.^{12,15,24}

Grid sensitivity of the configurations has been evaluated by comparison of the forces and moments of grids with various levels of refinement at low yaw angles. The Reynolds number for the grid sensitivity study was 3.2×10^5 , which is between the low and high range of configurations investigated throughout the rest of this work. The aspect ratio was 1.0 for the sensitivity study. Two different refinement techniques were applied:

1. uniform refinement, and
2. feature-based adaptation based on vorticity magnitude.

Feature-based adaptation capability has been introduced into FUN3D for overset grids by Shenoy.^{13,25} In this technique, flow features of interest (such as separated shear layers and shed vortices) can be resolved while reducing the number of grid points in regions of smooth flow. The baseline grid had 3.7 million nodes – a similar number of points as previous successful studies of rectangular prisms¹⁷ – while the finest grid had 8.5 million nodes.

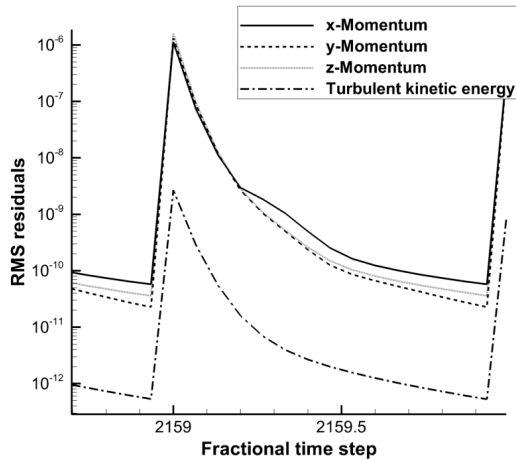


Figure 3: Typical convergence of momentum and turbulent kinetic energy RMS residuals.

III.B. Temporal convergence

As bluff body flows are highly unsteady, time-accurate computations are required. FUN3D applies a backwards differentiation scheme to achieve time accuracy between second-order and third-order. To ensure that the order of accuracy of the scheme is actually reached, a number of Newton subiterations employing pseudo time steps are applied to converge the solution within each physical time step. Equation 1 (see Biedron et al²⁶) defines the update equation for the vector of conserved variables \mathbf{Q} with the backwards differentiation scheme. In this equation, m is the pseudo time level, $\Delta\tau$ is the pseudo time step size, n is the physical time level, Δt is the physical time step size, \mathbf{R} is the residual vector, Ω is the dual cell volume, and θ_n are backwards differentiation coefficients.

$$\left[\left(\frac{\Omega}{\Delta\tau} + \frac{\Omega\theta_{n+1}}{\Delta t} \right) \mathbf{I} - \frac{\partial \mathbf{R}^m}{\partial \mathbf{Q}} \right] \Delta \mathbf{Q}^m = \mathbf{R}^m - \frac{\Omega\theta_{n+1}}{\Delta t} (\mathbf{Q}^m - \mathbf{Q}^n) - \frac{\Omega\theta_{n-1}}{\Delta t} (\mathbf{Q}^{n-1} - \mathbf{Q}^n) - \frac{\Omega\theta_{n-2}}{\Delta t} (\mathbf{Q}^{n-2} - \mathbf{Q}^n) - \dots \quad (1)$$

During a convergent time step, $\Delta \mathbf{Q}^m \rightarrow 0$ and $\mathbf{Q}^{m+1} \rightarrow \mathbf{Q}^{n+1}$. Unlike in steady simulations, convergence of time-accurate computations does not imply that the residual goes to zero during the Newton subiteration process, but rather to a small finite value that depends on Δt and represents the change in the flow solution during the physical time step. Thus, leveling of the residuals to a finite value indicates that the Newton subiterations have converged. In this work, 15–20 subiterations were used with a CFL number of 35 to ensure that the RMS residuals of momentum and turbulent kinetic energy converge three orders of magnitude and begin to level out when plotted on a log scale. Typical convergence of these residuals during a time step is illustrated in Fig. 3. It was found that the number of subiterations and CFL number for temporal convergence did not change significantly across the different cases and flow conditions evaluated.

IV. Results

IV.A. Drag comparisons with experimental data

The present numerical analysis approach has been previously validated against infinite cylinder experiments in the subcritical regime, $Re_D = 3900$.¹² The drag coefficient, shedding frequency, and separation location were all well within the error bounds of experimental measurements in that low- Re_D study. Because the

tethered loads application typically involves larger Reynolds numbers, the current work focuses on transitional and supercritical flows. The computations are compared against experimental data at $\beta = 0^\circ$ and 90° , as other orientations are not available in the literature for short finite cylinders. Figure 4(a) presents the drag coefficients of the present computations in normal flow ($\beta = 0^\circ$) compared with the experimental data of Wieselsberger⁶ and with the prior computations of Lynch and Smith.¹² Here, the drag force is normalized by the planform area LD . It is apparent from this figure that the agreement with experimental data is excellent in the supercritical regime. Furthermore, in both the transitional and supercritical regimes, the difference in drag coefficient between the two different aspect ratios is minimal. This is in agreement with the experimental findings of Zdravkovich et al.,⁷ who found that the drag coefficient is insensitive to aspect ratio below $L/D = 5$.

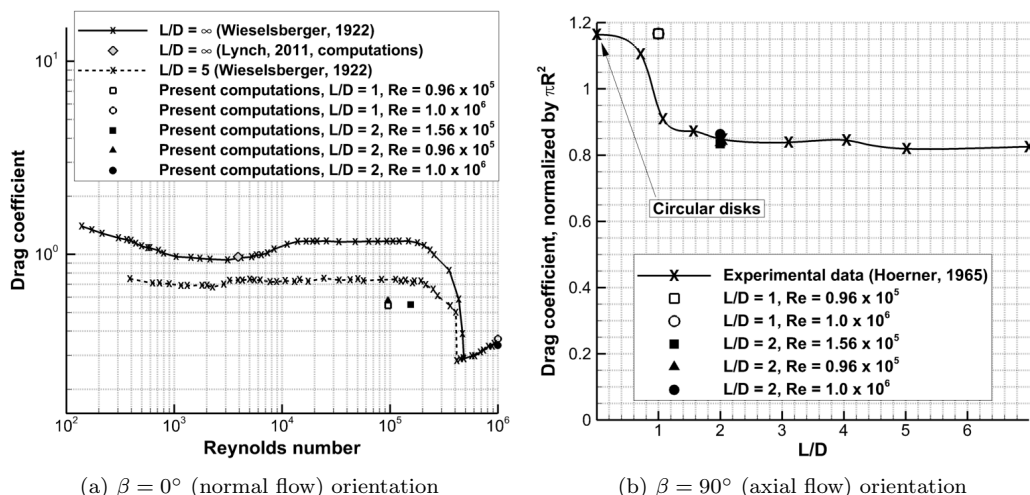


Figure 4: Comparison of the current computations in normal and axial flow configurations with experimental data by Wieselsberger,⁶ Hoerner,⁸ and previous computations by Lynch and Smith.¹²

The finite drag predictions at lower Reynolds numbers are somewhat lower than the experimental data, with only minor variation when increasing the Reynolds number from 0.96×10^5 to 1.56×10^5 . However, they are comparable to the experimental drag in the transitional regime, which occurs at a somewhat higher Reynolds number in the experiments. Hoerner⁸ indicated that boundary layer transition may occur at different Reynolds numbers depending on the surface roughness and wind tunnel turbulence level. Considering the excellent correlation at subcritical¹² and supercritical Reynolds numbers, it is clear that the hybrid RANS-LES turbulence approach is able to accurately predict drag of wake-dominated flows at Reynolds numbers outside of the boundary-layer transitional regime. However, the RANS model, which is active in the boundary layer, does not predict transition. As a result, the range of Reynolds numbers over which this change takes place is larger than in the experiments. For the applications noted in the Introduction, fully turbulent flows are primarily of interest, and boundary layer transition is of minimal importance. Nonetheless, the effects of boundary layer transition as it relates to other aerodynamic interest will be discussed later in this paper.

Figure 4(b) illustrates the drag in the axial-flow orientation, as compared with experimental data from Hoerner⁸ for circular disks and finite cylinders. Note that the drag force here is normalized by the area $\frac{\pi}{4}D^2$, corresponding to the frontal area in the axial configuration (in the normal configuration, LD is the frontal area). This figure indicates that in axial flow, there is no sensitivity of the drag to Reynolds number, at least over the range of Reynolds numbers evaluated here. This result is perhaps unsurprising, as in this configuration forced separation occurs at the sharp edges of the flat face, whereas in the normal configuration, separation from the curvilinear face depends on the boundary layer and wake turbulence characteristics. The present computations at $L/D = 1$ give drag comparable to circular disks in the experimental data. The Hoerner data indicates that there is a sharp drop in drag near this aspect ratio corresponding to a change in the shear layer reattachment behavior. As the shear layer reattachment distance is sensitive to the freestream turbulence level in bluff body flows,²⁷ it is not unusual for the change in shear layer behavior to occur at a

different aspect ratio depending on the wind tunnel or conditions in the numerical study. The drag coefficient at $L/D = 2$ is consistent with the experimental data.

Figure 5 highlights the differences in shear layer behavior for the two different aspect ratios in axial flow. Time-averaged contours of pressure coefficient and streamlines are depicted in a top-down view of each case. Separation is forced by the sharp edges of the front face, promoting the formation of low-pressure, vortical bubbles that draw the outer flow back towards the surface. For $L/D = 2$, reattachment occurs on the curvilinear face of the cylinder downstream, but it remains separated for $L/D = 1$, as the cylinder length is not sufficient to allow reattachment. Shear layer reattachment is accompanied by a significant pressure recovery, resulting in significantly lower base pressure and drag for the higher aspect ratio. Reattachment occurs abruptly as the aspect ratio is increased, which is the reason for the sudden decrease in drag in Fig. 4(b) between $L/D = 1$ and 2.

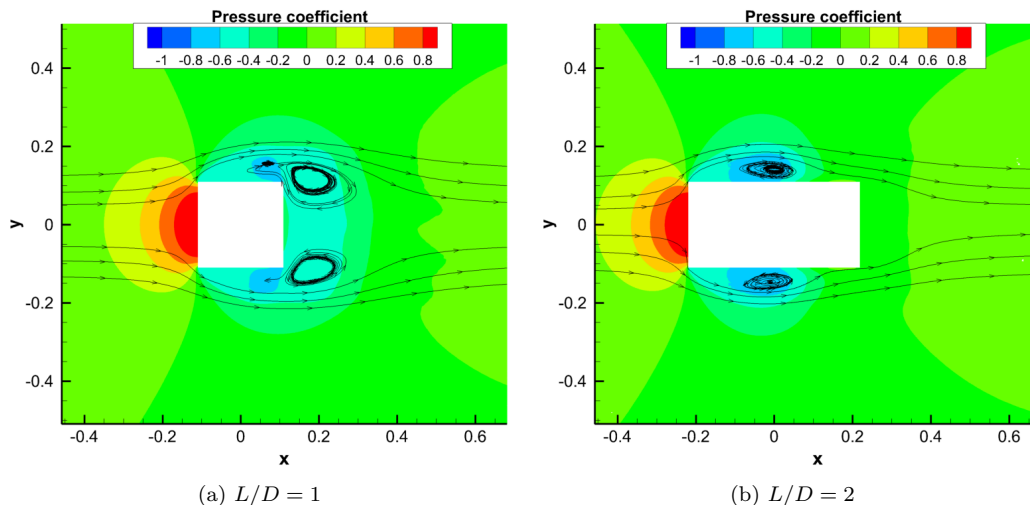


Figure 5: Time-averaged contours of pressure coefficient and streamlines in a top-down view for the axial flow condition.

IV.B. Forces and moments in other orientations

Figure 6 details the influence of changing yaw angle on the time-averaged forces and moments for different aspect ratios and Reynolds numbers. All forces are normalized by the reference area LD , while the yaw moment is normalized by the reference area LD and the reference length D . The level of unsteadiness in each case is indicated by vertical bars, the magnitude of which represents the root-mean-square of the fluctuations in each quantity.

The drag coefficient behavior is illustrated in Fig. 6(a). For each of the two aspect ratios, the most significant changes with Reynolds number occur near $\beta = 0^\circ$, the normal flow condition. As has been demonstrated in Fig. 4(a), the lower- Re_D cases are in the midst of a transitional regime at $\beta = 0^\circ$, while the higher- Re_D cases are supercritical. The difference in turbulence properties of the wake manifests itself as a decrease in drag at low yaw angles in the supercritical regime. However, the influence of Reynolds number on drag decreases as the yaw angle is increased; for $\beta = 30^\circ$ and above, only minor differences in drag exist for a given aspect ratio at different Reynolds numbers. This behavior indicates that, for moderate to high yaw angles, fixed separation from sharp edges becomes the dominant factor that determines overall drag, and that this behavior is relatively independent of Reynolds number.

Significant differences in drag exist between the two aspect ratios for moderate to large yaw angles. Some of these differences are related to shear layer reattachment behavior in the axial flow condition, as indicated by Fig. 4(b). However, it should be noted that, due to the normalization by LD , the differences in dimensional drag at higher yaw angles are not actually as large as the differences in drag coefficient. The variations in reattachment behavior are discussed in detail in a later section.

Except for at very low yaw angles, the side force and yaw moment are also primarily dependent on aspect ratio instead of Reynolds number. The side force for the $L/D = 1$ cylinder is especially sensitive to minor

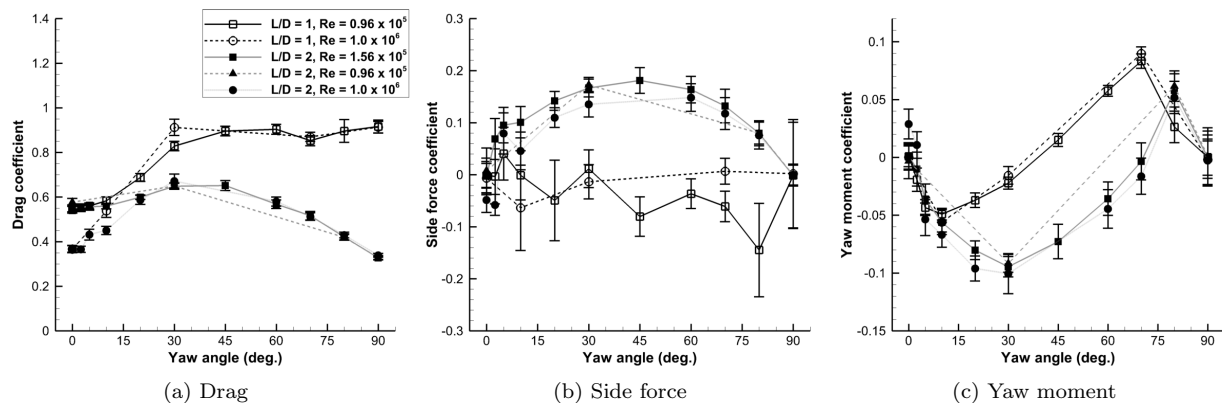


Figure 6: Time-averaged force and moment coefficients over the range $\beta = 0^\circ - 90^\circ$, with vertical bars denoting RMS fluctuations.

flow changes, which is evident in the numerous changes in slope across the range of β and the significant levels of unsteadiness. This sensitivity also results in larger changes with Reynolds number than in the other quantities, though similar sensitivity of the side force coefficient is apparent at both transitional and supercritical Reynolds numbers. The trends in yaw moment are similar for both aspect ratios, but with reversals occurring at different yaw angles. These reversals are related to changes in shear layer behavior on the sides of the cylinder. Similar effects have been characterized in the case of two-dimensional rectangular geometries by other authors.^{3, 28, 29} Only minor changes of the yaw moment with Reynolds number are observed.

IV.C. Unsteady flow characteristics

For many applications of bluff body aerodynamics, the mean flow behavior is not the only concern. Bluff body flows are inherently unsteady due to the shed wake, even when the configurations are static or quasi-steady. The unsteadiness is particularly important for applications in which the dynamic response of the bluff body is sought, for instance in the helicopter tethered loads application³⁰ and vortex-induced vibration of bridges, tall buildings, towers, and cables.³¹

Figure 6 provides an indication of the fluctuation magnitudes for each of the force and moment coefficients in the form of vertical bars, but it is easier to see the trends by plotting the fluctuations themselves with the mean value subtracted out. Such a comparison is presented in Fig. 7. The largest fluctuations occur in the side force coefficients for $L/D = 1$, particularly between $\beta = 0^\circ$ and 30° and $\beta > 70^\circ$. These fluctuations are especially significant when compared with the mean side force coefficient magnitude. Fluctuation magnitudes in all three coefficients are, in general, more closely correlated with aspect ratio than Reynolds number, but this trend does not always hold. For instance, the fluctuations in drag at yaw angles below 45° follow the opposite behavior, with fluctuation magnitudes correlated with Reynolds number instead of aspect ratio. The same trends were observed in the mean drag coefficient, which suggests that separation location on the curved cylinder surface influences not only the drag but also the unsteady fluctuations in drag.

In addition to the fluctuation magnitudes, the frequencies also represent an important aspect of unsteady flow. In order to accurately capture the relevant frequencies, it is necessary to apply large-eddy simulation in the wake,^{22, 32} as has been done in this work. Figure 8 depicts the power spectrum for velocity magnitude, V , measured $4D$ downstream of the $L/D = 1$ cylinder at $Re_D = 1.0 \times 10^6$. The frequency is plotted in terms of the non-dimensional Strouhal frequency St . While a dominant shedding frequency can be identified, the spectrum is broadly distributed across a range of frequencies. A significant amount of high-frequency content is also resolved by large-eddy simulation. These resolved frequencies drop off with a slope of approximately $-5/3$ on a log-log scale, eventually leveling out at scales too fine to be resolved by the grid.

When the dominant Strouhal frequency is plotted for each of the cases, as in Fig. 9, the range extends from 0.14 to 0.27, and clearly identifiable trends related to aspect ratio, yaw angle, or Reynolds number are absent. Experimental frequency data by Zdravkovich et al⁷ for a cylinder with $L/D = 2$ at $\beta = 0^\circ$, in the

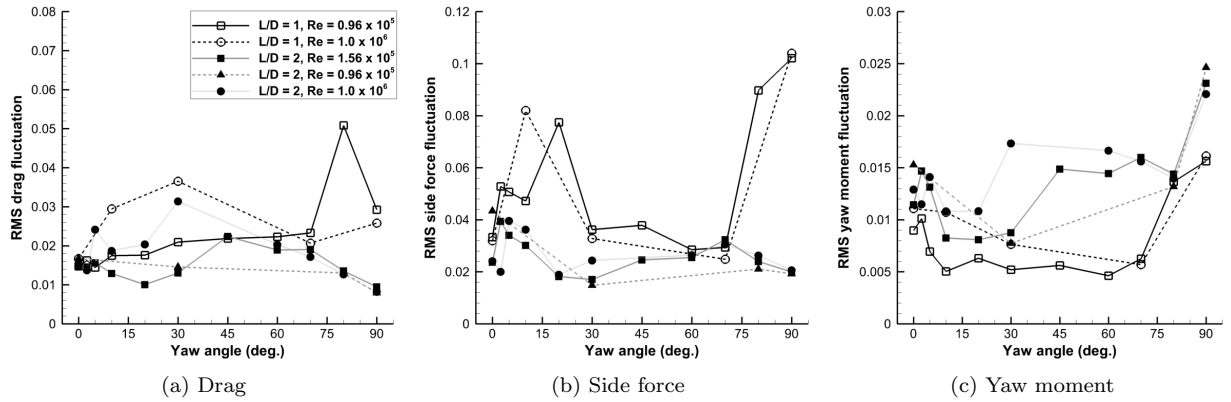


Figure 7: RMS of force and moment coefficient fluctuations over the range $\beta = 0^\circ - 90^\circ$.

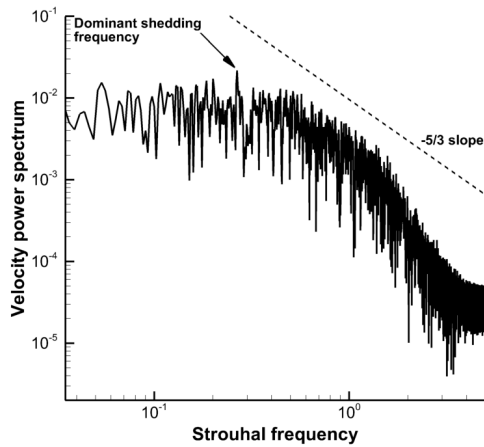


Figure 8: Power spectrum of velocity magnitude, $L/D = 1, Re_D = 1.0 \times 10^6, \beta = 0^\circ$.

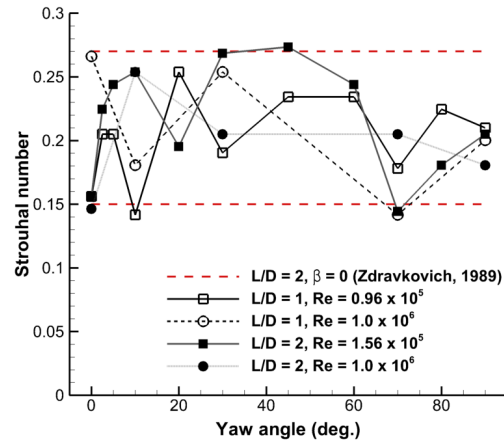


Figure 9: Dominant Strouhal frequencies. Experimental data from Zdravkovich et al.⁷

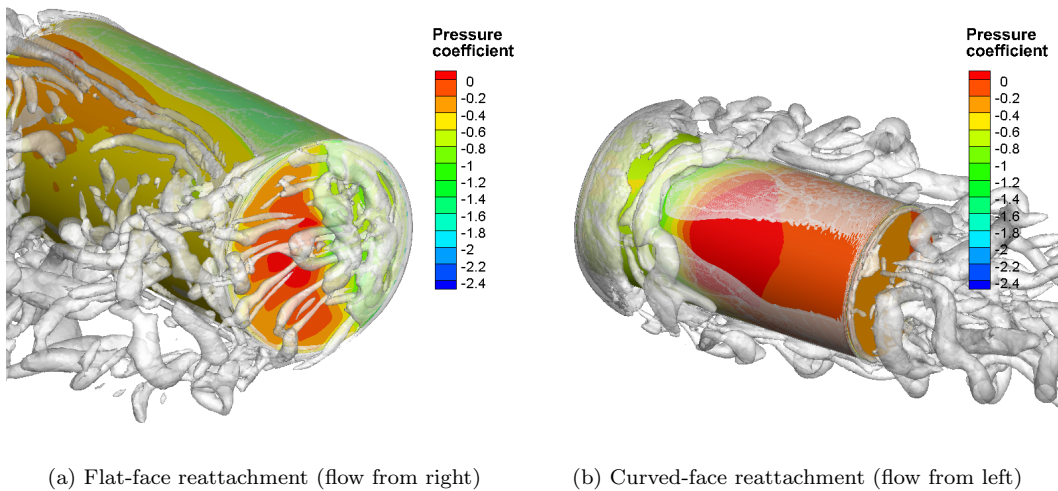


Figure 10: Unsteady flow snapshots during reattachment on flat and curved cylinder faces.

range $1.1 \times 10^5 \leq Re_D \leq 2.1 \times 10^5$, is also included in this figure. They observed a large range in measured Strouhal numbers, for the same flow conditions, from trial to trial; the range is illustrated by the red dashed lines in the figure. The significant variability in the experimental measurements of the Strouhal number was attributed to the highly three-dimensional and turbulent nature of the flow fields, resulting in broad, multimodal frequency spectra similar to those of the present computations. Similar behaviors have also been observed for three-dimensional rectangular prisms.²³ However, the typical two-dimensional cylinder Strouhal number of 0.2 is roughly in the center of the range of variability, so it is a reasonable approximation that may be applied in dynamic simulation models, provided vortex shedding lock-in to body dynamic frequencies is not a concern.

IV.D. Time-averaged pressures

The significant unsteadiness and complex turbulent structures in flows about finite cylinders can make it challenging to study the phenomena that primarily influence the mean forces and moments. To illustrate this point, Fig. 10 presents flow field visualizations at specific points in time for $L/D = 2$ at low (Fig. 10(a)) and high (Fig. 10(b)) yaw angles. Iso-surfaces of Q -criterion in the wake are rendered as smoke, while the surface is colored by contours of pressure coefficient. In both snapshots, there exist complex, highly three-dimensional turbulent structures that are resolved by large-eddy simulation. The significant three-dimensional nature of these structures and interaction between the vortices shed from the curved surface and the ends are responsible for the significant variation in dominant shedding frequency, as described in the previous section.

In addition, both figures also illustrate shear layer reattachment; in Fig. 10(a) this phenomenon occurs on the flat face while in Fig. 10(b) it occurs on the curved face. Shear layer reattachment is characterized by a low-pressure separation bubble, followed by a sudden increase in pressure and then a region of attached flow. The shear layer often breaks up into vortices before reattaching, as in Fig. 10(a), which results in unsteady variations in the reattachment point and unsteady interactions between other vortices and the surface.

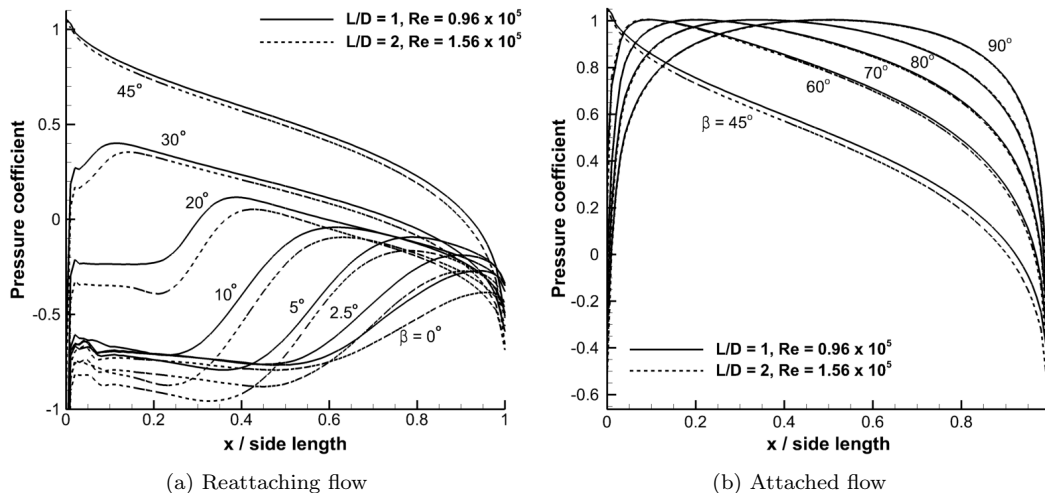


Figure 11: Pressure distributions for reattaching and attached flow on flat cylinder faces.

In order to extract the mean behavior, which is important for understanding the factors driving the mean forces and moments, the flow fields themselves have been time averaged. Figure 11 presents time-averaged reattaching- and attached-flow pressure distributions along central slices of the flat faces. For clarity, only the results from a subset of the cases are presented in this figure. The time-averaging process produces smooth pressure distributions which provide insight into the behavior of the mean forces and moments. The separation bubble and attached flow distributions are apparent in Fig. 11(a). Reattachment on the flat faces occurs even at $\beta = 0^\circ$, when the flat faces are parallel to the flow. Increasing the yaw angle moves the reattachment point forward and increases the maximum pressure coefficient at reattachment. At low yaw angles, the pressure in the separation bubble changes only slightly, but it subsequently begins to

increase rapidly, At $\beta = 45^\circ$, the stagnation point occurs at the corner of the flat face, and the separation bubble vanishes completely. Reattachment behavior has been demonstrated by Greenwell³ and Robertson²⁷ to drastically influence the side force and yaw moment for rectangular bluff bodies, and similar influences are apparent for finite cylinders. For example, the rapidly-changing separation bubble size and pressure distribution in Fig. 11(a) produces the rapid changes in yaw moment apparent in Fig. 6(c). The qualitative aspects of the reattachment pressure distributions are very similar among finite cylinders and two- and three-dimensional rectangular bluff bodies.^{3,23,27}

Further increasing the yaw angle, as represented in Fig. 11(b), results in the stagnation point moving from the curved face to the flat face. The pressure coefficient is 1.0 at the stagnation point, but it moves from the edge of the flat face to the center as the yaw angle is increased to 90° . The fully-attached pressure distribution is somewhat simpler than the reattaching pressure distribution, in that the maximum pressure remains constant and there is no separation bubble. As a result, the attached flow distribution can be characterized by the stagnation point location, x_0 . Meanwhile, the reattaching pressure distribution requires four parameters: c_{p_b} , the base pressure coefficient; c_{p_s} , the separation bubble pressure coefficient; c_{p_M} , the maximum pressure coefficient at reattachment, and x_M , the distance from the edge to the location of c_{p_M} . These parameters are highlighted in Fig. 12, which depicts typical reattaching- and attached-flow pressure distributions.

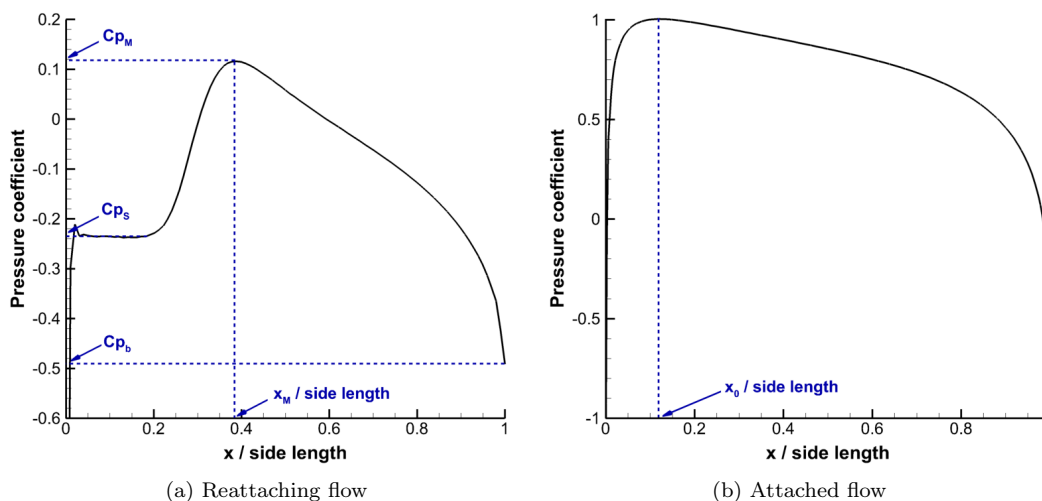


Figure 12: Typical pressure distributions and definition of empirical modeling parameters.

V. Empirical Modeling of Quasi-Steady Behavior

Due to the significant nonlinearities in bluff body flows, including transition, separation, and reattachment, simplified analytical theories generally not available. This fact poses significant difficulties in developing reduced-order models for pilot training, certification, and stability analysis. As a result, costly suites of experiments, flight tests, or high-fidelity numerical simulations are typically required to build a database of quasi-steady force and moment information for each geometry under consideration.³⁰ Empirical modeling presents an alternative to analytical modeling, with similar benefits to applications such as flight simulation which require a method with low computational cost. Some work has been done in this area by Greenwell³ in the case of two- and three-dimensional rectangular bluff bodies. The current work aims to develop similar empirical models for the quasi-steady behavior of finite cylinders, to understand where there exist similarities or differences with the prior work on rectangular bluff bodies, and to quantify sensitivities with respect to surface type, Reynolds number, and aspect ratio.

One key parameter related to the reattachment behavior is the angle at which reattachment on a given face begins to occur. For this analysis, it is more instructive to consider the incidence angle ϕ – the angle of the flow relative to a given face – instead of the yaw angle. By plotting the reattachment distance x_M normalized by the diameter as a function of the incidence angle, it is possible to develop empirical models for the reattachment angle which very closely fit the data, as demonstrated in Fig. 13. These figures clearly

indicate that x_M does not depend on the aspect ratio or the Reynolds number, but rather on the type of face on which reattachment occurs (flat or curved). Though similar trends exist for both types of face, x_M is larger for a given incidence angle when reattachment occurs on the curved cylinder face as opposed to one of the flat faces. Prior work^{3,23} has indicated x_M follows a similar trend for two- and three-dimensional rectangular prisms, but with x_M larger than either of the empirical fits in Fig. 13. The incidence angle at which reattachment begins to occur on a particular face, or ϕ_R , can be determined from these empirical models by setting x_M equal to the length of the face and reading the incidence angle from the curve fit.

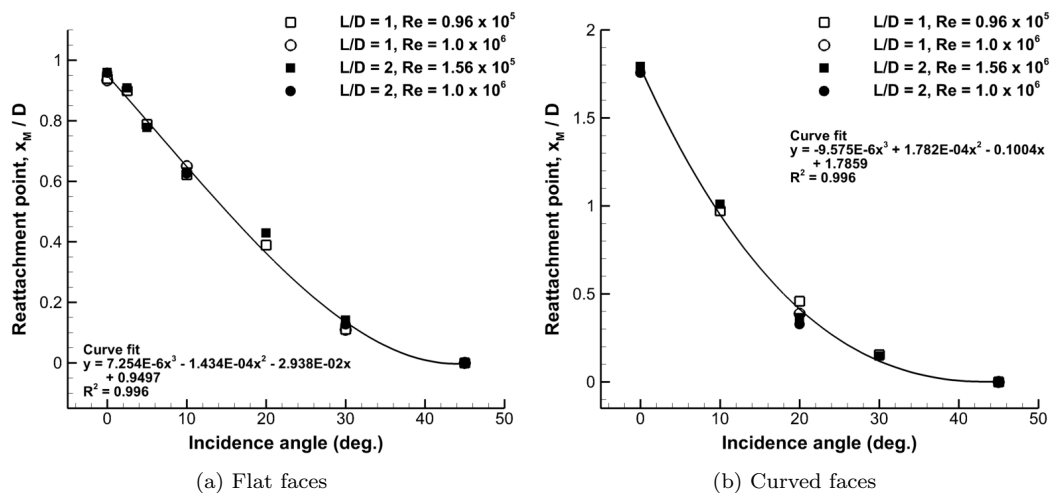


Figure 13: Reattachment distance as a function of incidence angle, normalized by D , for reattachment on flat and curved faces.

Figure 14 presents empirical models of the four reattachment pressure distribution parameters. Many of them collapse onto a single curve when normalized in the proper way. The incidence angle, for instance, is normalized by first subtracting ϕ_R and then dividing by 45° . The pressure coefficients are normalized by subtracting c_{pb} at $\phi = 0^\circ$, or $c_{pb, \phi=0}$, and dividing by $(1 - c_{pb, \phi=0})$. When normalized in this manner, it is notable that the variation in x_M collapses onto a single quadratic curve with $R^2 = 0.97$, and the relationship becomes independent of surface type, canonical geometry type (it applies equally well to cylinders as 2-D and 3-D rectangular bluff bodies^{23,27}), aspect ratio, and Reynolds number. If ϕ_R is not subtracted out, as in Fig. 13, then the curve fits differ with surface type. This result indicates that these geometric differences have a significant effect on ϕ_R , but the variation of x_M with ϕ after reattachment begins follows a similar trend in all cases. Therefore, the model provided in Fig. 13 should be used to determine ϕ_R , and the model in Fig. 14(a) may be applied once ϕ_R is known.

The maximum pressure coefficient during reattachment, c_{pM} , exhibits similar independence when normalized appropriately. All geometries evaluated collapse onto a single empirical curve with $R^2 = 0.96$, and c_{pM} increases with ϕ in a cubic relationship. The separation bubble pressure coefficient, c_{pS} , collapses in a similar manner, but in this case, there are differences with respect to the type of surface. For reattachment on flat faces (whether they are flat faces of cylinders or rectangular bluff bodies), c_{pS} can be modeled by an empirical curve fit with $R^2 = 0.98$. However, curved faces do not fit this trend; data for curved faces is highlighted in red in Fig. 14(c). In fact, c_{pS} on curved faces is found to depend not only on the incidence angle but also the aspect ratio and Reynolds number. The base pressure coefficient, c_{pb} , exhibits significant scatter and is not amenable to fitting by an empirical curve. However, note that this parameter is somewhat difficult to determine in the first place, as the pressure coefficient drops off rapidly at the aft end of the face (see Fig. 11(a)), and for most applications it is likely sufficient to assign it a constant representative value.

Figure 15 presents the variation of the stagnation point with incidence angle. As stagnation on a given face implies that reattachment does not occur on the same face, ϕ_R is not subtracted from the incidence angle for normalization in this case. Instead, since the transition from reattaching to fully-attached flow occurs at 45° , 45° is subtracted from the incidence angle instead of ϕ_R . Figure 15 demonstrates that x_0 , when normalized in this manner, also depends on the surface type. As was the case with c_{pS} , x_0 collapses onto a single empirical curve for flat faces, including both finite cylinders and rectangular bluff bodies. However,

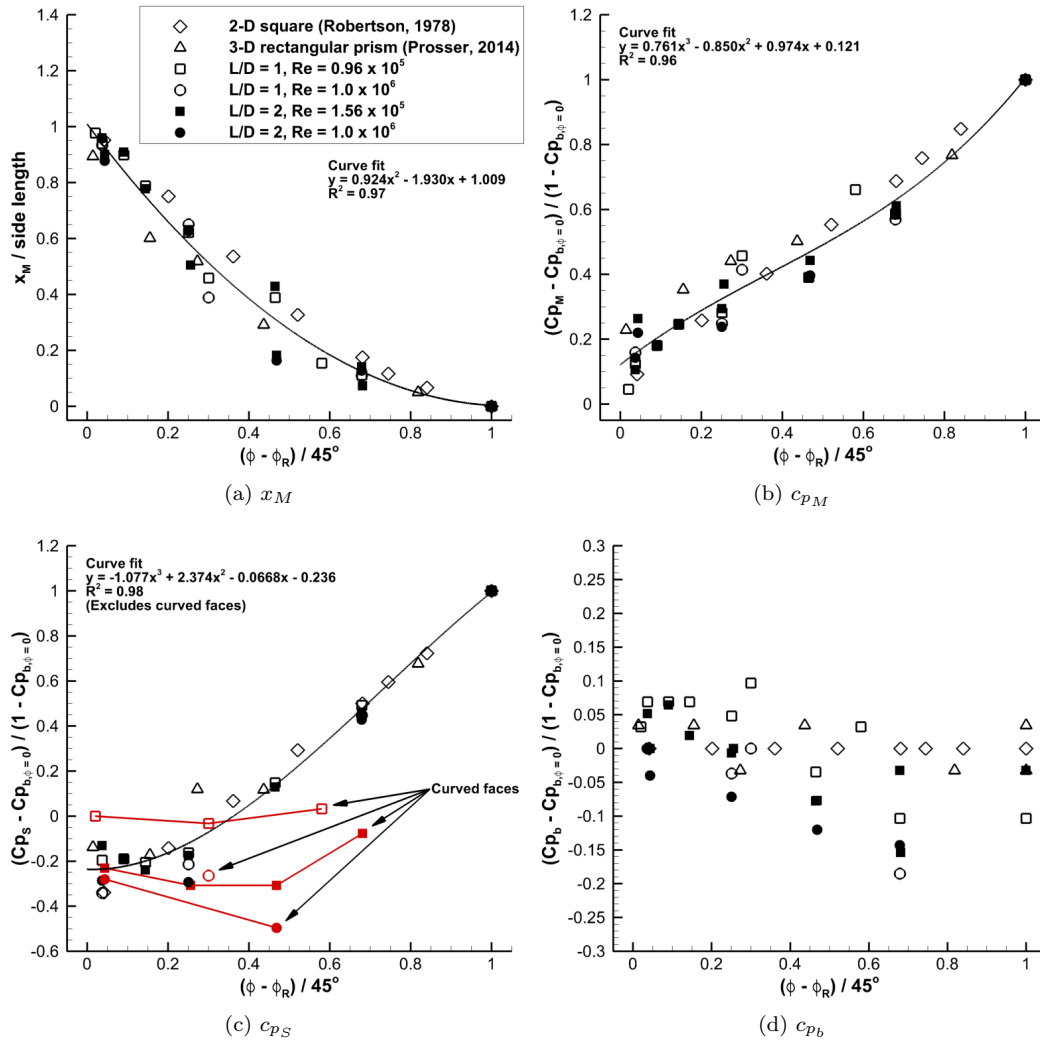


Figure 14: Reattachment parameter variations with ϕ and empirical curve fits.

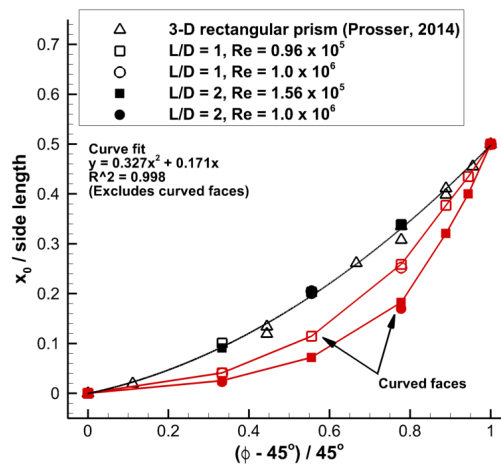


Figure 15: Variation of x_0 with ϕ and empirical curve fit.

curved-face stagnation (highlighted in red) does not fit the same trend. x_0 on curved faces is found to depend on L/D but not Re_D .

VI. Conclusions

In this work, the aerodynamics of finite cylinders with $L/D = 1$ and 2 in quasi-steady, or static, configurations have been investigated via high-fidelity numerical experiments. The purpose is to fill a significant gap in the literature in terms of the understanding and available data for these types of cylinders, particularly over a range of orientations which is necessary for many applications including tethered and parachute loads, crane operations, and freely-dropped bluff bodies. The computations have been validated by comparison with experimental data, where available, and sensitivities to grid refinement and flow conditions have been evaluated. The key findings of this work are as follows:

- Drag predictions from the hybrid RANS-LES method are highly accurate in the subcritical and supercritical regime. In the transitional regime, the drag is slightly underpredicted relative to available experimental data.
- Transition primarily affects the drag predictions for yaw angles below 30° but only influences the side force and yaw moment to a minor extent.
- The flow is highly unsteady and three-dimensional. Frequency-domain transformation of quantities in the wake results in a broad, multimodal spectrum. Because of these characteristics, clear trends in the dominant shedding frequency with respect to aspect ratio, yaw angle, or Reynolds number cannot be extracted, but $St = 0.2$ may be taken as a representative value.
- Due to the unsteadiness and turbulence, time-averaging the flow fields themselves is required to investigate the characteristics of the phenomena that produce the mean forces and moments. When this procedure is performed, clear qualitative trends are observed in the pressure distributions for faces on which shear layer reattachment or fully attached flow is present.
- The incidence angle at which reattachment begins to occur, or ϕ_R , can be correlated with surface type, curved or flat.
- The distance to reattachment, x_M , and the pressure coefficient at reattachment, c_{p_M} , may be modeled empirically as a function of incidence angle. These quantities have been found to be independent of geometry type, surface type, Reynolds number, and aspect ratio, provided the proper normalization is applied taking into account ϕ_R .
- The pressure coefficient in the separation bubble, c_{p_S} , and the stagnation point location, x_0 , have been found to depend on the surface type, curved or flat.
- Where possible, empirical curve fits have been developed and presented for predicting the reattachment and stagnation parameters.

Future development will include further correlation and validation of the force and moment predictions as well as the empirical curve fits established in this work. Additionally, other common canonical geometries will be evaluated. Methods to predict the mean forces and moments from the empirically-determined trends in shear layer behavior should be investigated, so that reasonable predictions for new bluff bodies can be made without the need for large suites of tests or numerical experiments.

VII. Acknowledgements

This research is funded through the U.S. Army/Navy/NASA Vertical Lift Rotorcraft Center of Excellence at Georgia Institute of Technology under Task 10 Dynamic-Aerodynamic Interactions of Bluff Bodies: Computational Investigations under the direction of Mahendra Bhagwat of AFDD, Agreement No. W911W6-11-2-0010. The authors would like to thank the technical points of contact of this project, Marty Moulton and Tom Thompson of AMRDEC and Gloria Yamauchi of NASA for their insights, as well as noted researchers in sling loads: Luigi Cicolani, Doug Greenwell, and Aviv Rosen.

The U.S. Government is authorized to reproduce and distribute reprints notwithstanding any copyright notation thereon. The views and conclusions contained in this document are those of the authors and should not be interpreted as representing the official policies, either expressed or implied, of the U.S. Government.

References

- ¹Zdravkovich, M., *Flow Around Circular Cylinders*, Vol. 2: Applications, Oxford University Press, 2003.
- ²Matheson, N., "The Stability of Portable Bridges Carried on Slings Beneath Helicopters," Tech. Rep. 154, Defence Science and Technology Organisation, 1980.
- ³Greenwell, D., "Modelling of Static Aerodynamics of Helicopter Underslung Loads," *The Aeronautical Journal*, Vol. 115, No. 1166, April 2011, pp. 201–219.
- ⁴Keener, E. R., Chapman, G. T., Cohen, L., and Taleghani, J., "Side Forces on a Tangent Ogive Forebody with a Fineness Ratio of 3.5 at High Angles of Attack and Mach Numbers from 0.1 to 0.7," Tech. Rep. NASA TM X-3437, National Aeronautics and Space Administration, 1977.
- ⁵Clarkson, M. H., Malcolm, G. N., Brittain, V. A., and Intemann, P. A., "Subsonic High-Angle-Of-Attack Aerodynamic Characteristics of a Cone and Cylinder with Triangular Cross Sections and a Cone with a Square Cross Section," Tech. Rep. NASA TM 84377, National Aeronautics and Space Administration, 1983.
- ⁶Wieselsberger, C., "Further Data on the Law of Liquid and Air Drag," *Phys. Zeit.*, Vol. 23, 1922, pp. 219–224, in German, reprinted in Zdravkovich.¹
- ⁷Zdravkovich, M., Brand, V., Mathew, G., and Weston, A., "Flow Past Short Cylinders with Two Free Ends," *Journal of Fluid Mechanics*, Vol. 203, June 1989, pp. 557–575.
- ⁸Hoerner, S., *Fluid-Dynamic Drag*, Hoerner Fluid Dynamics, Midland Park, NJ, 1958.
- ⁹Burnsall, W. J. and Loftin Jr., L. K., "Experimental Investigation of the Pressure Distribution about a Yawed Circular Cylinder in the Critical Reynolds Number Range," Tech. Rep. NACA TN-2463, National Advisory Committee for Aeronautics, 1951.
- ¹⁰Sears, W., "The Boundary Layer of Yawed Cylinders," *The Journal of Aeronautical Sciences*, Vol. 15, No. 1, 1948, pp. 49–52.
- ¹¹Ramberg, S., "The Effects of Yaw and Finite Length Upon Vortex Wakes of Stationary and Vibrating Circular Cylinders," *Journal of Fluid Mechanics*, Vol. 128, March 1983, pp. 81–107.
- ¹²Lynch, C. E. and Smith, M. J., "Extension and Exploration of a Hybrid Turbulence Model on Unstructured Grids," *AIAA Journal*, Vol. 49, No. 11, Nov. 2011, pp. 2585–2590.
- ¹³Shenoy, R., Smith, M., and Park, M., "Unstructured Overset Mesh Adaptation with Turbulence Modeling for Unsteady Aerodynamic Interactions," *Journal of Aircraft*, Vol. 51, No. 1, Jan. 2014.
- ¹⁴Anderson, W., Rausch, R., and Bonhaus, D., "Implicit/Multigrid Algorithms for Incompressible Turbulent Flows on Unstructured Grids," *Journal of Computational Physics*, Vol. 128, No. 2, 1996, pp. 391–408.
- ¹⁵Smith, M. J., Liggett, N. D., and Koukol, B. C., "Aerodynamics of Airfoils at High and Reverse Angles of Attack," *AIAA Journal of Aircraft*, Vol. 48, No. 6, November–December 2011, pp. 2012–2023.
- ¹⁶Cicolani, L. S., Cone, A., Theron, J., Robinson, L. D., Lusardi, J., Tischler, M. B., Rosen, A., and Raz, R., "Flight Test and Simulation of a Cargo Container Slung Load in Forward Flight," *Journal of the American Helicopter Society*, Vol. 54, No. 3, July 2009, pp. 1–18.
- ¹⁷Prosser, D. T. and Smith, M. J., "Navier-Stokes-Based Dynamic Simulations of Sling Loads," *Proceedings of the 54th AIAA/ASCE/AHS/ASC Structures, Structural Dynamics, and Materials Conference*, No. AIAA-2013-1922, Boston, Massachusetts, April 8 – April 11 2013.
- ¹⁸Theron, J. N., Gordon, R., Rosen, A., Cicolani, L., Duque, E. P., and Halsey, R. H., "Simulation of Helicopter Slung Load Aerodynamics: Wind Tunnel Validation of Two Computational Fluid Dynamics Codes," *AIAA 36th Fluid Dynamics Conference and Exhibit*, No. AIAA-2006-3374, San Francisco, CA, June 5–8, 2006, pp. 1–14.
- ¹⁹Chorin, A., "A Numerical Method for Solving Incompressible Viscous Flow Problems," *Journal of Computational Physics*, Vol. 2, No. 1, 1967, pp. 12–26.
- ²⁰Noack, R., "SUGGAR: A General Capability for Moving Body Overset Grid Assembly," *17th Computational Fluid Dynamics Conference*, No. AIAA-2005-5117, American Institute of Aeronautics and Astronautics, Toronto, Ontario, June 2005.
- ²¹Noack, R., "DiRTlib: A Library to Add an Overset Capability to Your Flow Solver," *17th Computational Fluid Dynamics Conference*, No. AIAA-2005-5116, American Institute of Aeronautics and Astronautics, Toronto, Ontario, June 2005.
- ²²Shenoy, R., Holmes, M., Smith, M. J., and Komerath, N., "Scaling Evaluations on the Drag of a Hub System," *Journal of the American Helicopter Society*, Vol. 58, No. 3, July 2013, pp. 1–13.
- ²³Prosser, D. T. and Smith, M. J., "Three-Dimensional Bluff Body Aerodynamics and Its Importance for Helicopter Sling Loads," *Proceedings of the 40th European Rotorcraft Forum*, Southampton, UK, Sept. 2–5 2014.
- ²⁴Liggett, N. and Smith, M. J., "Temporal Convergence Criteria for Time-Accurate Viscous Simulations of Separated Flows," *Computers & Fluids*, Vol. 66, 2012, pp. 140–156, doi: 10.1016/j.compfluid.2012.06.010.
- ²⁵Shenoy, R. and Smith, M., "Unstructured Overset Grid Adaptation for Rotorcraft Aerodynamic Interactions," *Proceedings of the 67th American Helicopter Society Annual Forum*, Virginia Beach, Virginia, May 3–5 2011.
- ²⁶Biedron, R. T., Vatsa, V. N., and Atkins, H. L., "Simulation of Unsteady Flows Using an Unstructured Navier-Stokes Solver on Moving and Stationary Grids," *Proceedings of the 23rd AIAA Applied Aerodynamics Conference*, No. AIAA 2005-5093, Toronto, Ontario, Canada, June 6–9 2005.

²⁷Robertson, J., Wedding, J., Peterka, J., and Cermak, J., "Wall Pressures of Separation – Reattachment Flow on a Square Prism in Uniform Flow," *Journal of Wind Engineering and Industrial Aerodynamics*, Vol. 2, No. 4, January 1978, pp. 345–359.

²⁸Norberg, C., "Flow around Rectangular Cylinders: Pressure Forces and Wake Frequencies," *Journal of Wind Engineering and Industrial Aerodynamics*, Vol. 49, No. 1–3, December 1993, pp. 187–196.

²⁹Prosser, D. T. and Smith, M. J., "Characterization of Flow Around Rectangular Bluff Bodies at Angle of Attack," *Physics Letters A*, Vol. 376, No. 45, 2012, pp. 3204 – 3207.

³⁰Prosser, D. T. and Smith, M. J., "A Novel, High Fidelity 6-DoF Simulation Model for Tethered Load Dynamics," *Proceedings of the 70th American Helicopter Society Annual Forum*, Montréal, Québec, May 20 – 22 2014.

³¹Matsumoto, M., "Vortex Shedding of Bluff Bodies: A Review," *Journal of Fluids and Structures*, Vol. 13, No. 7–8, October 1999, pp. 791–811.

³²Smith, M., Cook, J., Sánchez-Rocha, M., Shenoy, R., and Menon, S., "Improved Prediction of Complex Rotorcraft Aerodynamics," *Proceedings of the 69th American Helicopter Society Annual Forum*, Phoenix, Arizona, May 21–23 2013.